

Activation of peroxydisulfate to degrade the Orange II dye by nitrogen-doped cyanobacterial carbon

Jun Chen^{a,b,*}, Layun Zhu^a, Shangqing Xia^a, Zhaoming Chen^a, Xue Li^a, Xiaohong Yang^a, Zihui Song^a, Yutong Wang^a, Zongsheng Zhan^a, Dongliang Shao^b

^aSchool of Biology, Food and Environment, Anhui Key Laboratory of Sewage Purification and Eco-restoration Materials, Hefei University, Hefei 230601, China, Tel.: +86 551 62158405; Fax: +86 551 62158406; email: chenjun@hfu.edu.cn (J. Chen), Tel.: +86 551 62158150; Fax: +86 551 62158406; emails: 2966705708@qq.com (L. Zhu), 784773012@qq.com (S. Xia), 934147780@qq.com (Z. Chen), 1411094217@qq.com (X. Li), 2352845847@qq.com (X. Yang), 2283010192@qq.com (Z. Song), 1297607049@qq.com (Y. Wang), Tel.: +86 551 62158409; Fax: +86 551 62158406; email: 3046482480@qq.com (Z. Zhan)
^bPostdoctoral Workstation, Anhui Guoke Testing Technology Co., Ltd., Hefei 230041, China, Tel.: +86 551 63355905; Fax: +86 551 63355905; email: 315048402@qq.com

Received 31 January 2023; Accepted 14 May 2023

ABSTRACT

The activated cyanobacterial carbon (ACC) prepared from Chaohu Lake cyanobacteria was used as a carrier for nitrogen doping to synthesize nitrogen-doped activated cyanobacterial carbon (N@ACC), a highly efficient activation material. N@ACC was found to be an effective catalyst for the degradation of Orange II (OII) dye by activating peroxydisulfate (PMS). Characterization of N@ACC showed that it had a larger specific surface area (159.12 m²/g) than ACC and an average particle size of 3.28 nm. N@ACC also contained various functional groups such as C=O, C=N, and –OH. To optimize the degradation of OII, the reaction conditions of the N@ACC activated PMS system were adjusted. The N@ACC activated PMS system was able to achieve a degradation rate of 98.8% for OII (100 mg/L) within 35 min, which was significantly higher than the rate achieved by the ACC activated PMS system (19.5%). The degradation reaction followed first-order kinetics and indicated a combined free radical mechanism. Compared to ACC, N@ACC contained a higher content of nitrogen, specifically pyridinic and graphitic nitrogen. The results showed that introducing nitrogen would refactor the structure of raw carbon, regulate its properties, and create new active sites for the degradation of pollutants. Moreover, N@ACC does not need metallic elements to improve PMS degradation efficiency. Therefore, the synthesis of N@ACC could be used as a new way to activate PMS.

Keywords: Activated cyanobacterial carbon; Nitrogen doping; Peroxydisulfate; Orange II

1. Introduction

Biochar has attracted much attention due to its advantages of a green economy and ideal immobilization. Biochar has seen rapid development in catalytic materials due to its diverse composition, hierarchical porous structure, low cost, and environmental friendliness. Simultaneously,

designing and modifying biochar through various physical or chemical methods has been attempted to improve its performance. Different modification methods affect the physical and chemical properties of biochar. Generally, metal biochar, formed by loading metals with biochar, such as platinum, silver, manganese, iron, and cobalt, has been widely studied as an effective material. However,

* Corresponding author.

the secondary pollution caused by metals must be considered. Therefore, it is essential to improve some functional characteristics of biochar as needed [1–3]. Carbon materials have attracted widespread attention as a new type of non-metallic activator [4], however, raw carbon has always shown unsatisfactory catalytic performance. Therefore, unremitting efforts have been made to break the inertia and improve their catalytic performance through chemical modification [5,6]. In the realm of activators for advanced oxidation techniques like peroxymonosulfate (PMS), carbon-based nanomaterials are particularly appealing due to their effective catalytic properties and eco-friendliness. Heteroatom doping, particularly nitrogen doping, has emerged as a simple and effective approach for adjusting the electronic properties of the sp^2 hybridized carbon framework and creating additional active sites. During the nitrogen doping process, three typical nitrogen-bond structures are usually formed in the carbon network. Various carbon-based materials, including graphene oxide, carbon nanotubes, and nanodiamonds, have been utilized in water treatment and have demonstrated impressive capabilities for handling pollution issues [7–13]. However, raw carbon catalysts show poor stability in heterogeneous reactions. Consequently, doping heteroatoms with nitrogen, sulfur, phosphorus, or boron in the carbon honeycomb network is an effective strategy to solve this problem [14–20].

The primary contents of this study are as follows: (1) synthesizing nitrogen-doped activated cyanobacterial carbon (N@ACC) using a simple method, (2) characterizing and analyzing the physicochemical properties of N@ACC, (3) exploring the influencing factors of PMS activated by N@ACC on Orange II (OII) dye, and (4) investigating and analyzing the mechanisms of reaction.

2. Materials and methods

2.1. Materials

Activated cyanobacterial carbon (ACC) was obtained using cyanobacteria collected from Chaohu Lake as the raw material. The percentages of elements C, H, N, and O in cyanobacteria were 46.68%, 7.36%, 7.02%, and 38.94%, respectively. PMS ($KHSO_5 \cdot 0.5KHSO_4 \cdot 0.5K_2SO_4$), potassium iodide (KI), potassium chloride (KCl), potassium bromide (KBr), potassium ferrate (K_2FeO_4), hydrochloric acid (HCl), sodium hydroxide (NaOH), ethanol (C_2H_6O), methanol (CH_3OH , denoted as MeOH), tert-butyl alcohol ($(CH_3)_3COH$, denoted as TBA), and furfuryl alcohol ($C_5H_6O_2$, denoted as FFA) were purchased from Aladdin Reagent Co., Ltd., China. Additionally, urea, OII ($C_{16}H_{11}N_2NaO_4S$), Congo red ($C_{32}H_{22}N_6Na_2O_6S_2$, denoted as CR), and rhodamine B ($C_{28}H_{31}ClN_2O_3$, denoted as RB) were purchased from Sinopharm Chemical Reagent Co., Ltd., China. All reagents were analytical grade.

2.2. Preparation of N@ACC

Appropriate amounts of dry cyanobacteria powder were placed in a crucible. The tube furnace was heated up to 500°C and maintained for 6 h, with a heating rate of 10°C/min, while under N_2 protection. After maintaining the carbonization temperature for 6 h, the furnace was allowed to cool. The carbonized powder was then passed through

a 100-mesh sieve and soaked in 1 mol/L of HCl for 12 h. Following this, the ash was removed, and the powder was washed with deionized water, dried under neutral conditions, and stored for further use. Additionally, 5 g of ACC was taken and soaked in K_2FeO_4 (solid–liquid ratio = 1 g: 100 mL, 0.1 mol/L). Then, it was soaked in urea solution for 24 h (urea/ACC = 2, w/w), dried at 60°C, and ground into fine particles. Then, the fine particles were calcined at 800°C for 2 h (heating rate = 10°C/min) and acid washed. Finally, they were washed with deionized water several times, dried at 60°C, and ground through a 200-mesh sieve to obtain the remaining N@ACC black powder.

2.3. Analytical methods

The scanning electron microscopy (SEM) and transmission electron microscopy (TEM) images of the samples were observed using S-4800 cold-field emission (Hitachi, Japan) and FEI-TALOS-F200X (Fei, America), respectively. The specific surface area and pore size of the particles in the samples were determined from the N_2 adsorption/desorption curves using a fully automated surface and porosity tester (Quantachrome, America). Additionally, the zeta potential was measured at different pH using a zeta analyzer (Zetasizer Nano-ZS 90, Malvern, America). The X-ray diffraction (XRD) patterns and X-ray photoelectron spectrometer (XPS) were recorded using an X-ray diffractometer (TD-3500, Tongda, China) and a spectrometer (K-Alpha, Thermo Fisher, America). The samples were analyzed using Fourier-transform infrared (FT-IR) spectroscopy with an FT-IR spectrometer (Nicolet iS50 Continuum, Thermo Fisher, America), and Raman spectra were obtained using a confocal laser micro-Raman spectrometer (DXR, Thermo Fisher, America). To measure the absorbance of OII, CR, and RB, an ultraviolet spectrophotometer (Shanghai Yuanxi Instrument Co., Ltd., China) was used, with wavelengths of 484 nm, 488 nm, and 570 nm, respectively. The radicals in the samples were detected by using electron paramagnetic resonance (EPR, Bruker A300, Germany) in the presence of 5,5-dimethyl-1-pyrroline-1-oxide (DMPO) and 2,2,6,6-tetramethyl-4-piperidone (TEMP).

3. Results and discussion

3.1. Material characterization

3.1.1. SEM and TEM

The surface morphologies of ACC and N@ACC observed using SEM and TEM are shown in Fig. 1. The surface of ACC was relatively smooth with a compact structure. However, the surface of N@ACC was looser with a large number of void structures, providing more reaction area and contact sites for the subsequent reactions. The surface area, porous structure, and diameter of the pores are the main physical factors affecting their interaction with organic pollutants. Modifying the pore structure can create medium and micropores, which enhance the reaction with organic pollutants. The reaction of organic pollutants mostly takes place in the microporous structure. However, the strong adsorption of organic matter in the micropores results in irreversible adsorption, which can significantly reduce the efficiency of

pollutant removal. The microporous structure also affects the adsorption, desorption, and migration of organic pollutants in the environment, making it essential for pollutant penetration [21–23].

3.1.2. BET and zeta potential

The reaction mainly occurred on the surface of the activator due to the activation of PMS. Therefore, the specific surface area of N@ACC was determined for further understanding. The specific surface areas of ACC and N@ACC

were 97.46 and 159.12 m²/g, respectively. The pore volumes of ACC and N@ACC were 0.057 and 0.0709 cm³/g, respectively. Therefore, the pore volume of N@ACC was greater than ACC. Good porosity and pore size are the keys to single doping. The Brunauer–Emmett–Teller surface area and N@ACC pore volume according to the nitrogen adsorption isotherm are shown in Fig. 2. The N@ACC adsorption isotherm was a typical type IV isotherm according to the IUPAC classification, with P/P₀ having an H₄ hysteresis loop between 0.4 and 1.0, implying the presence of micro- and mesopores in N@ACC, with an approximate average pore

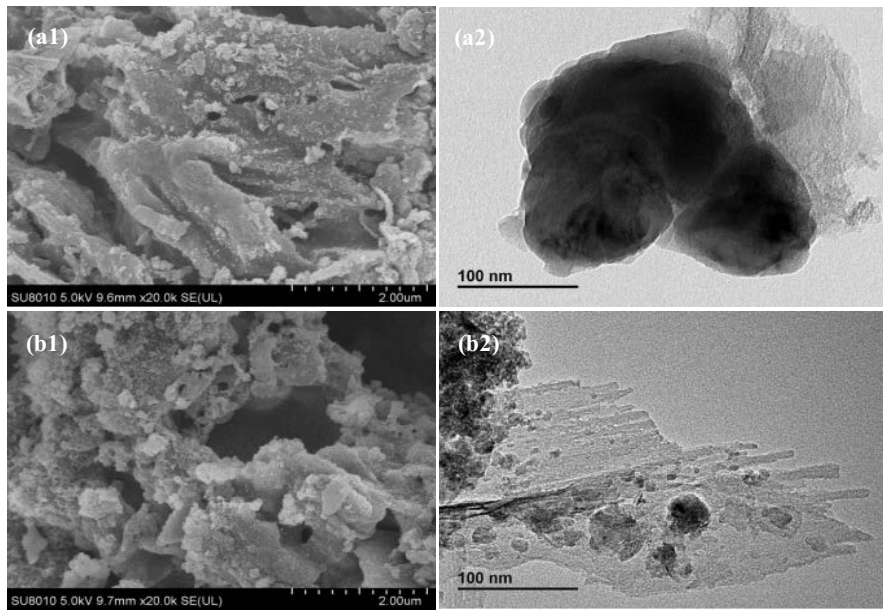


Fig. 1. Scanning electron microscopy and transmission electron microscopy images of (a1, a2) ACC and (b1, b2) N@ACC.

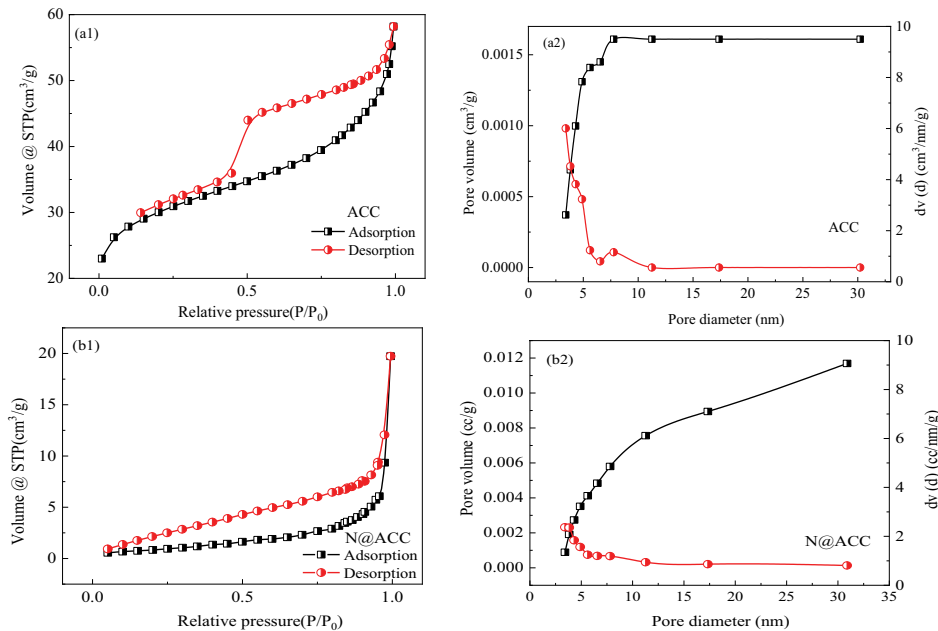


Fig. 2. N₂ adsorption–desorption isotherms and Barrett–Joyner–Halenda desorption size distribution of (a1, a2) ACC and (b1, b2) N@ACC.

size of 3.28 nm. Furthermore, the zeta potentials of N@ACC and ACC measured at different pH are shown in Fig. 3. The value of the point of zero charge (pH_{pzc}) was 4.10 for N@ACC. The results showed that N@ACC had higher zero potential and stronger adaptability in environmental applications than ACC, which had $\text{pH}_{\text{pzc}} = 2.32$.

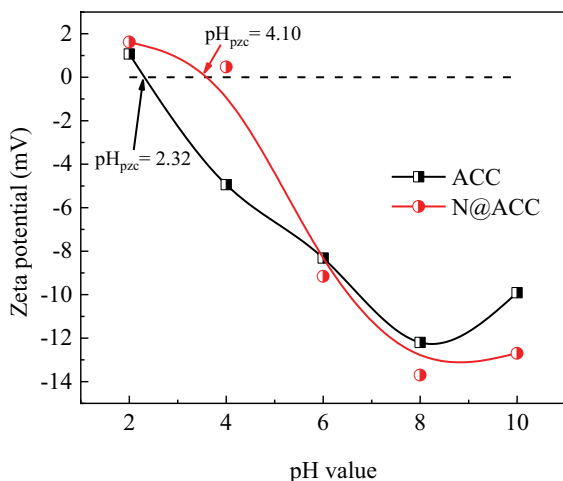


Fig. 3. Zeta potentials of (a) ACC and (b) N@ACC.

3.1.3. XRD, XPS, FT-IR, and Raman analysis

The XRD spectra of ACC and N@ACC are shown in Fig. 4a. Sharp (011) diffraction peaks appeared at 26.8° for ACC and N@ACC, indicating that they had graphitized structures. However, the diffraction peak intensity for N@ACC was significantly enhanced compared with ACC, indicating a good order and the formation of an ordered layered structure for N@ACC. Furthermore, the XPS spectra are shown in Fig. 4b. ACC showed O1s (351 eV) and C1s (293 eV) elemental signals. Additionally, N@ACC showed an N1s peak at 378 eV, and the presence of O1s and C1s elemental signals. In addition, FT-IR analysis was done to explore the effect of nitrogen doping on the surface properties of materials, as shown in Fig. 4c. ACC and N@ACC displayed similar infrared absorption peaks. They showed C–O and –OH stretching vibration infrared absorption peaks at 1044 and 3435 cm^{-1} , respectively. Additionally, they showed C=C and C=N stretching vibration absorption peaks at 1628 and 2252 cm^{-1} , respectively. Additionally, Fig. 4d illustrates the outcomes of the Raman spectral analysis conducted on ACC and N@ACC. The D- and G-bands for both materials were observed at 1344 and 1589 cm^{-1} , respectively. The $I_{\text{D}}/I_{\text{G}}$ intensity ratio for N@ACC was 1.01, indicating the presence of significant C–N structural defects and nitrogen atom doping in the carbon lattice.

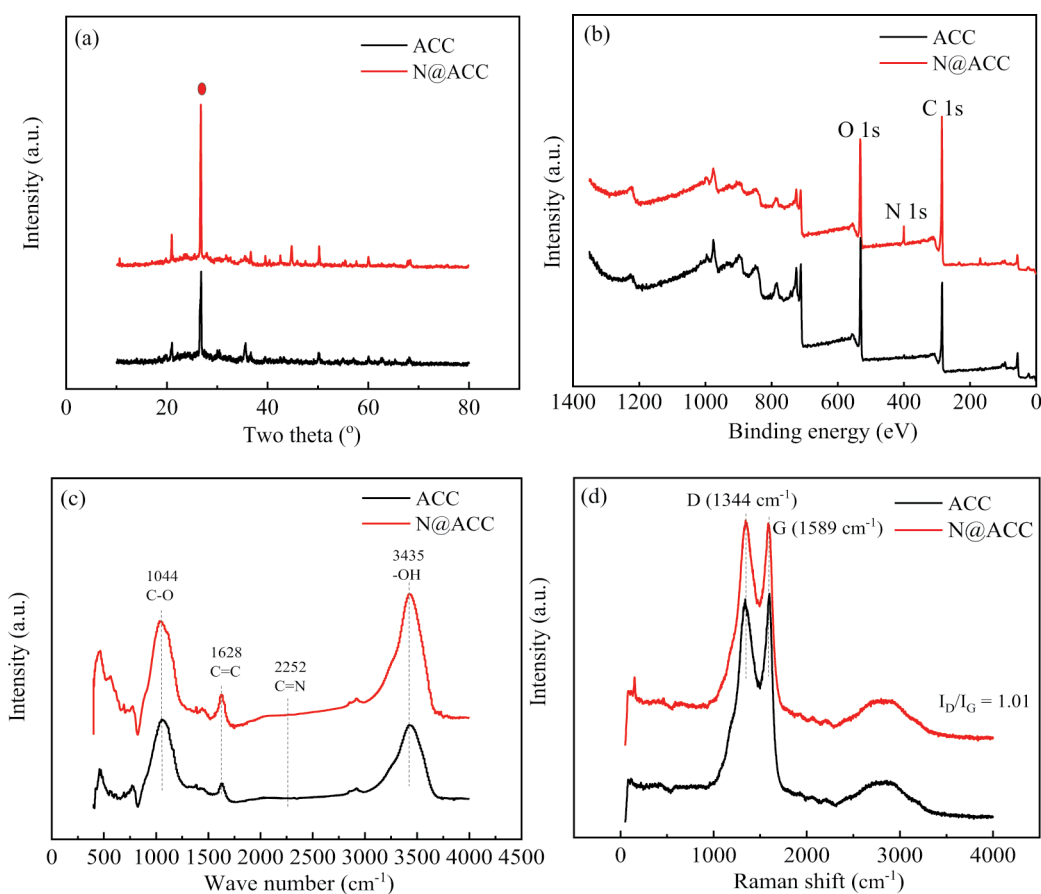


Fig. 4. (a) X-ray diffraction, (b) X-ray photoelectron spectroscopy, (c) Fourier-transform infrared spectroscopy, and (d) Raman analysis of ACC and N@ACC.

3.2. Effect of reaction conditions in the N@ACC/PMS system on OII degradation

The batch experiments were conducted in a 250 mL glass conical flask containing 100 mL of OII (100 mg/L) at an oscillation frequency of 110/min. The effects of different reaction conditions were studied in the N@ACC/PMS system on OII degradation.

3.2.1. Effect of N@ACC dosage

Initially, a constant temperature of 25°C and at pH 6, the effect of N@ACC dosage (0.1–0.4 g) on OII degradation is displayed in Fig. 5a. The OII degradation rate increased from 56.6% to 98.8% when the N@ACC dosage increased from 0.1 to 0.2 g. The increase in the amount of N@ACC provided more surface reaction sites, thereby improving the OII degradation rate and accelerating the reaction rate. However, the OII degradation did not continue to improve with a further increase in the N@ACC dosage. Continuing to increase to 0.3 or 0.4 g, the degradation rate has reached saturation and will no longer increase. Conversely, the degradation rates at 0.3 and 0.4 g were even lower than that at 0.2 g. Thus, the optimal N@ACC dosage was determined to be 0.2 g as it not only enhanced the degradation efficiency but also reduced the consumption of activator

materials. As shown in Fig. 5b, the kinetic simulation of the dosage showed that the degradation process conformed to the first-order kinetic process.

3.2.2. Effect of temperature and pH

The comparison of the degradation effect of OII at different temperatures (10°C, 25°C, and 40°C) are shown in Fig. 6a, it can be seen that the final degradation rate of OII at all three temperatures reached more than 98%. Additionally, the degradation rate of OII increased with temperature. Hence, the N@ACC/PMS system demonstrated a broad range of reaction temperature applications with degradation rates of 2.793, 2.808, and 2.815 mg/L·min at 10°C, 25°C, and 40°C, respectively. Moreover, the OII degradation rate by the N@ACC/PMS system increased with pH values ranging from 2 to 10. The color of the OII solution became lighter in an environment with a strong alkaline pH beyond 8. N@ACC had a pH_{pzc} of 4.1 and a rich cation exchange system. Thus, positive charges on the catalyst surface were more active. Therefore, the pH value of the reaction system in this study was set to 6, which was more abundant in anions and promoted the interconversion of positive and negative charges on the catalyst surface, leading to efficient electron transfer and accelerating the degradation of OII.

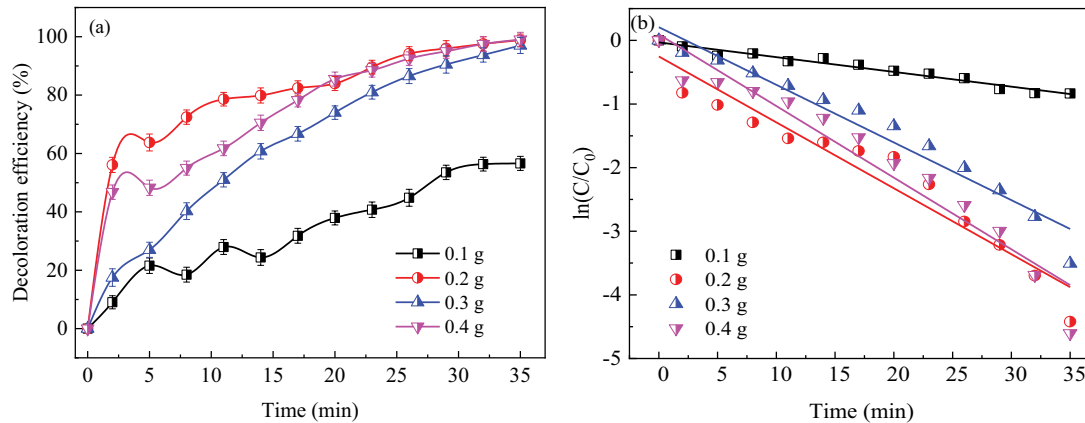


Fig. 5. Effect of different (a) dosages and (b) kinetic process on Orange II degradation in the N@ACC/PMS system.

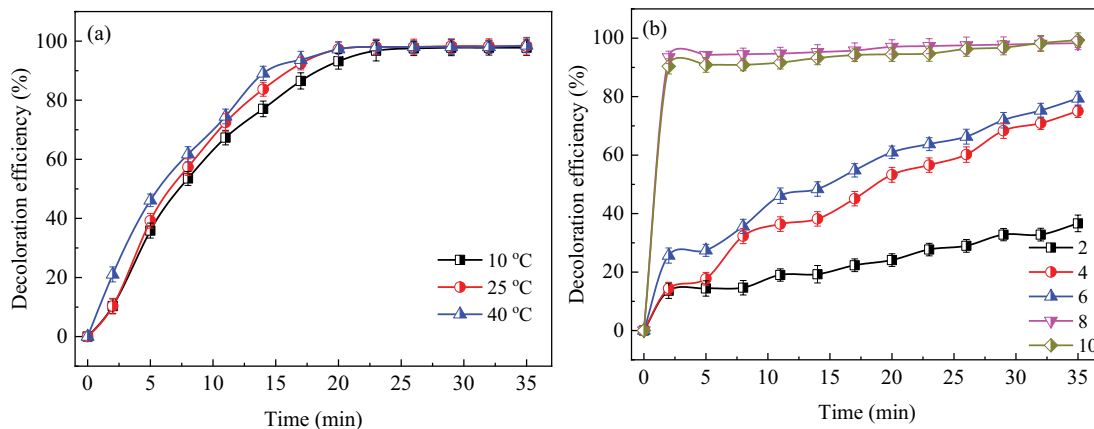


Fig. 6. Effect of different (a) temperatures and (b) initial pH on the Orange II degradation in the N@ACC/PMS system.

3.2.3. Effect of halogen ion

Halogen ions (I^- , Br^- , Cl^-) are common anions present in dye wastewater and may influence the reaction process [24]. As shown in Fig. 7a–c, the OII degradation rate decreased rapidly with increased halogen ion concentration. The OII degradation rate decreased to 0.021 L/mol·s when the I^- concentration in the solution was increased to 4.0 mmol/L. Additionally, the OII degradation rate decreased to 0.040 L/mol·s when the Br^- concentration in the solution was increased to 20 mmol/L. Furthermore, the OII degradation rate decreased to 0.042 L/mol·s when the Cl^- concentration in the solution was increased to 2.0 mol/L. The data concluded that halogen ions exerted an evident inhibition effect on the OII degradation by the N@ACC/PMS system. The inhibition effect of halogen ions on the degradation follows the order: $I^- > Br^- > Cl^-$. The competition for active sites of free radicals is the primary reason for the inhibitory effect of halogen ions on the degradation of OII. Previous research suggests that halogen ions can impede the electron transfer of oxidizing radicals during pollutant degradation, leading to competition for active sites and slowing down the oxidation of radicals. The presence of common halogen ions (I^- , Br^- , Cl^-) generates nonspecific oxidizing halogen radicals ($I_2^{\cdot-}$, $Br_2^{\cdot-}$, and $Cl_2^{\cdot-}$) by gaining energy and electrons during competition, which eventually diminishes the degradation of pollutants [25,26]. Hence, the presence of halogen elements hampers the degradation of OII dye pollutants by competing with active radicals for free sites.

3.2.4. Effect of different reaction systems

The OII degradation effect under different reaction systems with 0.2 g of N@ACC and 0.056 g of PMS was explored, as shown in Fig. 8. The adsorption effect of 0.2 g of ACC and 0.2 g of N@ACC was poor with less than 17.2% of OII removal rate. Additionally, the OII degradation rate by the ACC/PMS system was 19.5%, and there was no obvious activation effect. However, the OII degradation rate of the N@ACC/PMS system reached 98.8% within 14 min, realizing high-efficiency activation. Therefore, the results showed that N@ACC had the highest activation effect.

3.3. Analysis of the reaction mechanism

3.3.1. Inhibition experiment in the N@ACC/PMS system

MeOH, TBA, and FFA were selected as scavengers to determine the free radicals that play a role in the reaction

process. MeOH could react with $SO_4^{\cdot-}$ (9.7×10^8 L/mol·s) and $\cdot OH$ (3.2×10^6 L/mol·s) [27]. TBA is an efficient $\cdot OH$ scavenger since it has a high reaction rate constant for $\cdot OH$ ($3.8\text{--}7.6 \times 10^8$ L/mol·s). However, it is not sensitive to $SO_4^{\cdot-}$ since it has a low reaction rate constant or $SO_4^{\cdot-}$ ($4.0\text{--}9.1 \times 10^5$ L/mol·s). Therefore, TBA can be used as a probe for $\cdot OH$ [28–30]. Furthermore, FFA can react rapidly with 1O_2 , so it can be used as the capture agent for 1O_2 [31–33]. The experimental results are displayed in Fig. 9. The OII degradation rates were 33.3%, 40.5%, and 22.1% of adding MeOH, TBA, and FFA within 35 min in the N@ACC/PMS system, respectively. Therefore, the reaction rate was reduced, and the OII degradation was significantly inhibited compared with a blank group. $\cdot OH$, $SO_4^{\cdot-}$, and 1O_2 were the active substances that played roles in the reaction, and 1O_2 played the major role.

3.3.2. Test and analysis of EPR and XPS

The EPR test was conducted to further determine the free radicals that played a role in the reaction process. As shown in Fig. 10, the results indicated that as the reaction progressed, there were obvious $DMPO\cdot OH$, $DMPO\cdot SO_4^{\cdot-}$, and $TEMP\cdot ^1O_2$ characteristic peaks with 1:2:2:1, 1:1:1:1:1:1, and 1:1:1 intensity pattern in the N@ACC/PMS system, respectively, and the intensity gradually increased. The study confirmed that $\cdot OH$, $SO_4^{\cdot-}$, and 1O_2 were the free radicals involved in the reaction. Additionally, no significant characteristic peak was detected in comparison with the

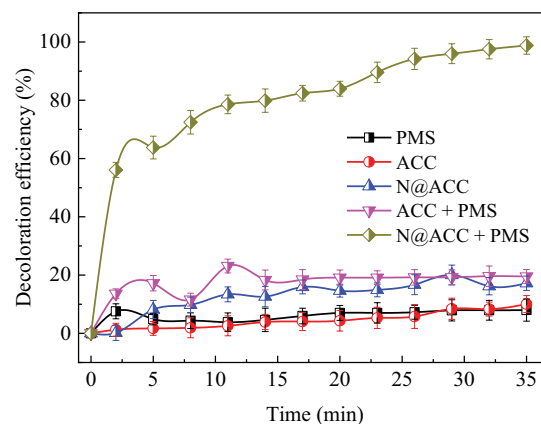


Fig. 8. Effect of different reaction systems on the Orange II degradation.

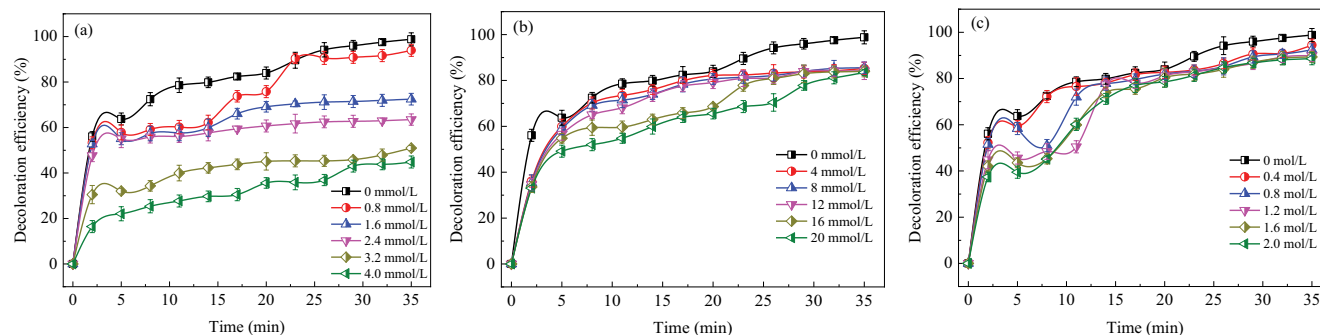


Fig. 7. Effect of different halogens (a) I^- , (b) Br^- , and (c) Cl^- on the Orange II degradation in the N@ACC/PMS system.

starting point of the reaction, indicating that the $^1\text{O}_2$ generated originated from PMS rather than the dissolved oxygen in the water. The results of the EPR analysis experimentally supported the inhibition hypothesis, indicating that N@ACC activation of PMS followed a combined mechanism of free and non-free radicals. Furthermore, XPS were analyzed, as shown in Fig. 11. Introducing nitrogen in raw carbon will destroy its structure, regulate its physical, chemical, and electrical properties, and create new active sites for various reactions [34–41]. The N and C elements were analyzed by XPS. As seen from Fig. 11a and c, four peaks which belonged to pyridinic N, pyrrolic N, graphitic N, and N oxides were fitted for 398.2, 399.9, 401.1, and 403.3 eV binding energies, respectively. The relative percentage of each nitrogen-based moiety had increased from ACC to N@ACC since the urea-derived nitrogen functionalization may have led to the change of nitrogen in ACC. Therefore, nitrogen might play an important role in promoting the activation of PMS. Pyridinic N at the N@ACC edge could be used as Lewis basic reaction site to induce the redox process, forming $\text{SO}_4^{\cdot-}$ and $^{\cdot}\text{OH}$ [42]. More importantly, since graphite N had a smaller covalent radius and higher electronegativity than carbon atoms, it would induce the transfer of electrons from adjacent carbon atoms to nitrogen atoms

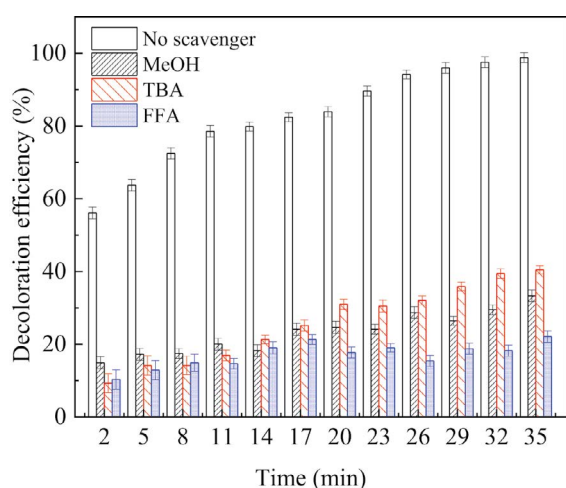


Fig. 9. Effect of different radical scavengers on Orange II degradation in the N@ACC/PMS system.

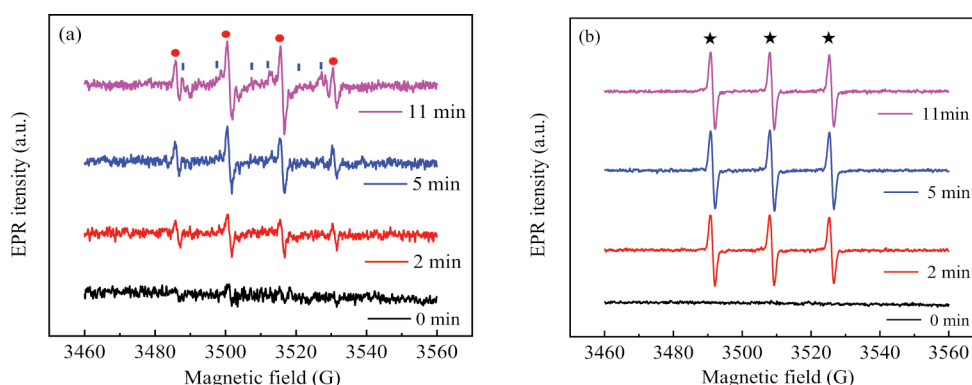


Fig. 10. EPR spectra for (a) DMPO and (b) TEMP of N@ACC/PMS system.

[43–45]. As seen in Fig. 11b and d, the peaks of C=N and C–N appeared for N@ACC after the urea-mediated nitrogen functionalization. The activation and participation of C=N and C–N in generating $^1\text{O}_2$ were considered to assist PMS. Additionally, the adjacent positively charged carbon atoms in C=O more easily accepted the nucleophilic addition of PMS, promoting the formation of $^1\text{O}_2$ [46]. Surface chemical groups of N@ACC before and after used in the N@ACC/PMS with the OII dye are analyzed in Fig. 11b and d, indicating no significant changes in the nitrogen and carbon group species on the surface. However, the content of pyridinic N decreased slightly from 6.22% to 5.32%, suggesting its role in the degradation of OII dye. As previously mentioned, pyridinic N at the N@ACC edge acted as a Lewis basic reaction site, inducing the redox process to produce $\text{SO}_4^{\cdot-}$ and $^{\cdot}\text{OH}$ [42]. The type and content of chemical groups on the surface of the N@ACC material remained stable after used in the reaction, indicating good stability and recyclability of the material from a microscopic perspective. The mechanism of activation of PMS by N@ACC is shown in Fig. 12, the proposed mechanism underlying the OII degradation reaction by the N@ACC/PMS system. The pH_{pzc} analysis indicated that the reduction in the electrostatic repulsion between PMS and N@ACC increased the probability of collision, promoting the transfer of electrons from the suspended state to C=O and producing various nitrogen active groups [47–53].

3.4. Reuse and wide application of N@ACC in the reaction

The reuse performance of N@ACC is explored in Fig. 13a. The OII degradation efficiency was 90.4% and 87.3% after one and two reuses, respectively, on recycling and drying N@ACC after the reaction. Although the degradation effect slightly decreased, it remained at a high level. Additionally, it had good activation performance for PMS after reuse. N@ACC was found to be widely utilized, as shown in Fig. 13b, demonstrating the degradation of three different dyes (OII, CR, and RB) under the same experimental conditions in the N@ACC/PMS system. The results revealed that the anionic dyes of OII and CR were degraded to more than 98% within 35 min, while the cationic dye RB was degraded only to 48.5%. The zeta potential analysis indicated that N@ACC had a cation exchange system that could specifically recognize anionic dyes, allowing for rapid transfer of

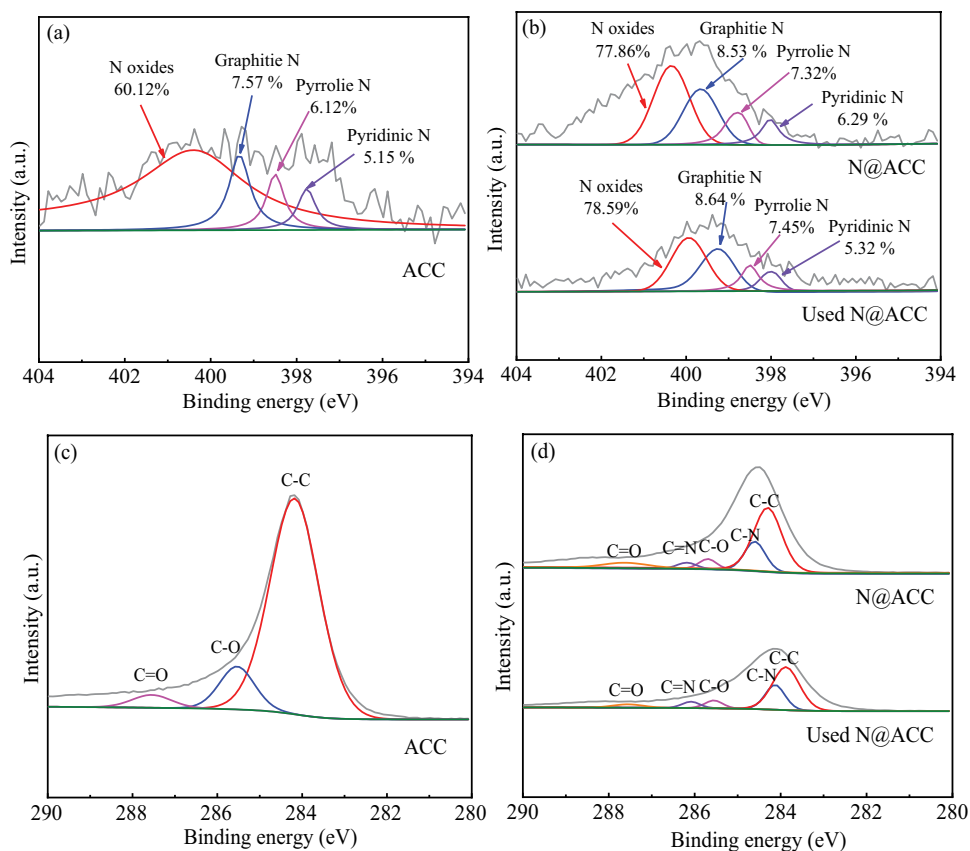


Fig. 11. High-resolution X-ray photoelectron spectra of N 1s for (a) ACC, (b) N@ACC and used N@ACC; C 1s for (c) ACC, (d) N@ACC and used N@ACC.

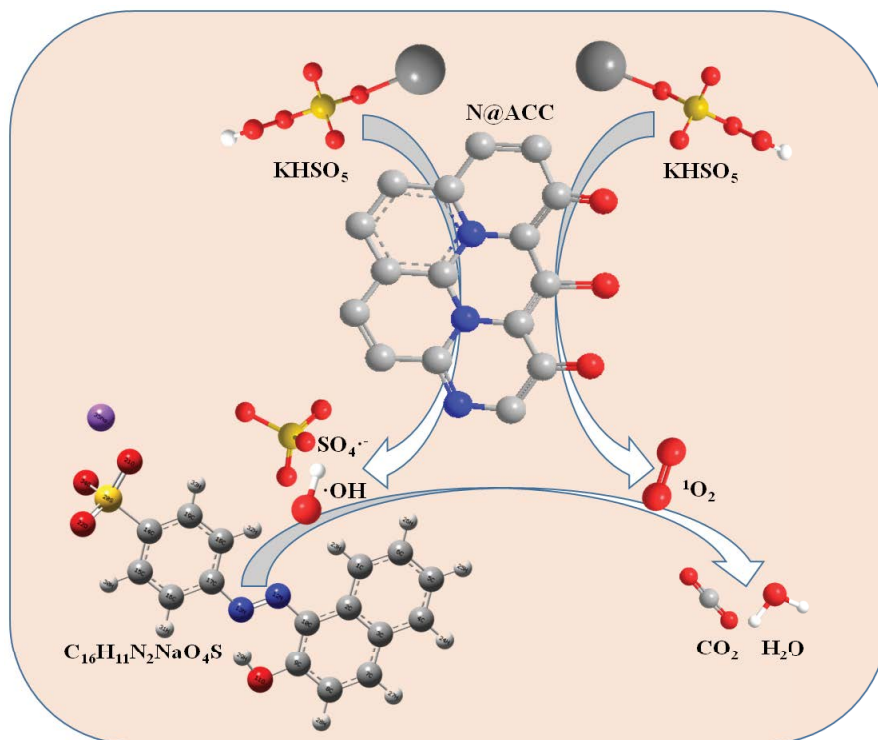


Fig. 12. Proposed mechanism underlying the Orange II degradation reaction in the N@ACC/PMS system.

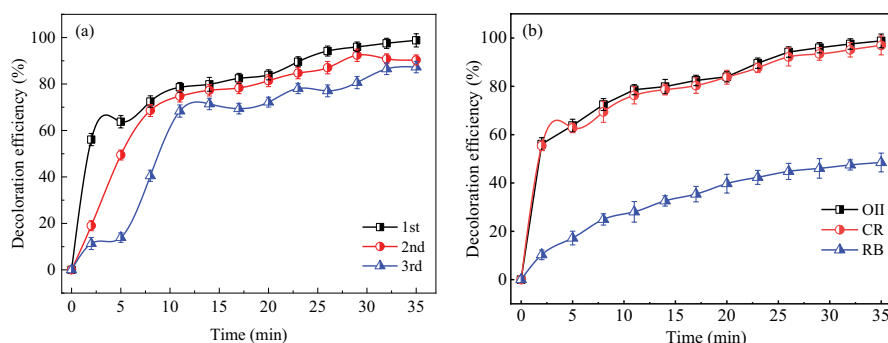


Fig. 13. (a) Reuse of the N@ACC for Orange II degradation and (b) degradation rate of different dye in the N@ACC/PMS system.

positive and negative charges on the surface of the material [54]. Therefore, the degradation of anionic dyes by N@ACC was more effective. Previous similar studies were compared to better illustrate the effect of N@ACC on the degradation of dyes. For example, Chen et al. [55] synthesized cyanobacterial carbon-supported nano-zero-valent iron materials to activate PMS and degrade OII, offering 98.3% degradation of OII. Khose et al. [56] developed a simple and highly effective method for synthesizing a boron nitride, chitosan, and graphene-based composite, which was used to degrade OII with a degradation rate of 57%. Overall, N@ACC exhibited good properties in activating PMS.

4. Conclusion

N@ACC was successfully prepared to achieve stable and efficient activation of cyanobacteria carbon. The OII removal rate degraded by the N@ACC/PMS system reached 98.8% within 35 min. Introducing nitrogen would refactor the ACC structure, regulate its properties, and create new active sites for the degradation of pollutants. The activated biochar material of N@ACC was prepared using urea and cyanobacteria, which could realize the resource utilization of cyanobacteria and efficient PMS activation.

Acknowledgments

This research was supported by Excellent Young Talent Support Project in Universities (gxyqZD2022076). Postdoctoral of Environmental Science and Engineering (934849). National Key R&D Program of China (2020YFC1908601, 2020YFC1908602). Graduate Innovation Project of Hefei University (21YCXL30). Demonstration Experiment Training Center Project (2018sxzx39). Science Development Fund Project of Hefei University (22040521004).

References

- [1] W.-D. Oh, Z. Dong, T.-T. Lim, Generation of sulfate radical through heterogeneous catalysis for organic contaminants removal: current development, challenges and prospects, *Appl. Catal., B*, 194 (2016) 169–201.
- [2] L. Hu, X. Yang, S. Dang, An easily recyclable Co/SBA-15 catalyst: heterogeneous activation of peroxymonosulfate for the degradation of phenol in water, *Appl. Catal., B*, 102 (2011) 19–26.
- [3] Y. Wang, H. Sun, X. Duan, H.M. Ang, M.O. Tade, S. Wang, A new magnetic nano zero-valent iron encapsulated in carbon spheres for oxidative degradation of phenol, *Appl. Catal., B*, 172–173 (2015) 73–81.
- [4] J. Liu, Z. Zhao, P. Shao, F. Cui, Activation of peroxymonosulfate with magnetic Fe_3O_4 - MnO_2 core-shell nanocomposites for 4-chlorophenol degradation, *Chem. Eng. J.*, 262 (2015) 854–861.
- [5] Y. Yang, J.J. Pignatello, J. Ma, W.A. Mitch, Comparison of halide impacts on the efficiency of contaminant degradation by sulfate and hydroxyl radical-based advanced oxidation processes (AOPs), *Environ. Sci. Technol.*, 48 (2014) 2344–2351.
- [6] H. Wang, W. Guo, B. Liu, Q. Wu, H. Luo, Q. Zhao, Q. Si, F. Sseguya, N. Ren, Edge-nitrogenated biochar for efficient peroxydisulfate activation: an electron transfer mechanism, *Water Res.*, 160 (2019) 405–414.
- [7] S. Wang, A comparative study of Fenton and Fenton-like reaction kinetics in decolourisation of wastewater, *Dyes Pigment.*, 76 (2008) 714–720.
- [8] S.B. Hammouda, F. Zhao, Z. Safaei, V. Srivastava, D. Lakshmi Ramasamy, S. Iftekhhar, S. Kalliola, M. Sillanpää, Degradation and mineralization of phenol in aqueous medium by heterogeneous monoperoxysulfate activation on nanostructured cobalt based-perovskite catalysts ACoO_3 (A = La, Ba, Sr and Ce): characterization, kinetics and mechanism study, *Appl. Catal., B*, 215 (2017) 60–73.
- [9] P.A. George, D.D. Dionysios, Degradation of organic contaminants in water with sulfate radicals generated by the conjunction of peroxymonosulfate with cobalt, *Environ. Sci. Technol.*, 37 (2003) 4790–4797.
- [10] Y. Wang, H. Sun, H.M. Ang, M.O. Tade, S. Wang, 3D-hierarchically structured MnO_2 for catalytic oxidation of phenol solutions by activation of peroxymonosulfate: structure dependence and mechanism, *Appl. Catal., B*, 164 (2015) 159–167.
- [11] E. Saputra, S. Muhammad, H. Sun, H.M. Ang, M.O. Tade, S. Wang, Different crystallographic one-dimensional MnO_2 nanomaterials and their superior performance in catalytic phenol degradation, *Environ. Sci. Technol.*, 47 (2013) 5882–5887.
- [12] P. Hu, M. Long, Cobalt-catalyzed sulfate radical-based advanced oxidation: a review on heterogeneous catalysts and applications, *Appl. Catal., B*, 181 (2016) 103–117.
- [13] S. Wang, H. Sun, H.M. Ang, M.O. Tade, Adsorptive remediation of environmental pollutants using novel graphene-based nanomaterials, *Chem. Eng. J.*, 226 (2013) 336–347.
- [14] T. Liu, Y. Li, Q. Du, J. Sun, Y. Jiao, G. Yang, Z. Wang, Y. Xia, W. Zhang, K. Wang, H. Zhu, D. Wu, Adsorption of methylene blue from aqueous solution by graphene, *Colloids Surf., B*, 90 (2012) 197–203.
- [15] D. Lin, B. Xing, Adsorption of phenolic compounds by carbon nanotubes: role of aromaticity and substitution of hydroxyl groups, *Environ. Sci. Technol.*, 42 (2008) 7254–7259.
- [16] W. Tian, H. Zhang, X. Duan, H. Sun, M.O. Tade, H.M. Ang, S. Wang, Nitrogen- and sulfur-codoped hierarchically porous carbon for adsorptive and oxidative removal of pharmaceutical contaminants, *ACS Appl. Mater. Interfaces*, 8 (2016) 7184–7193.
- [17] X. Duan, Z. Ao, H. Sun, S. Indrawirawan, Y. Wang, J. Kang, F. Liang, Z.H. Zhu, S. Wang, Nitrogen-doped graphene for

- generation and evolution of reactive radicals by metal-free catalysis, *ACS Appl. Mater. Interfaces*, 7 (2015) 4169–4178.
- [18] Y. Qian, X. Guo, Y. Zhang, Y. Peng, P. Sun, C.H. Huang, J. Niu, X. Zhou, J.C. Crittenden, Perfluorooctanoic acid degradation using UV-persulfate process: modeling of the degradation and chlorate formation, *Environ. Sci. Technol.*, 50 (2016) 772–781.
- [19] S. Indrawirawan, H. Sun, X. Duan, S. Wang, Low temperature combustion synthesis of nitrogen-doped graphene for metal-free catalytic oxidation, *J. Mater. Chem. A*, 3 (2015) 3432–3440.
- [20] S. Yang, L. Li, T. Xiao, Y. Zhang, D. Zheng, Promoting effect of ammonia modification on activated carbon catalyzed peroxymonosulfate oxidation, *Sep. Purif. Technol.*, 160 (2016) 81–88.
- [21] H. Cheng, E. Hu, Y. Hu, Impact of mineral micropores on transport and fate of organic contaminants: a review, *J. Contam. Hydrol.*, 129–130 (2012) 80–90.
- [22] P. Shah, A. Unnarkat, F. Patel, M. Shah, P. Shah, A comprehensive review on spinel based novel catalysts for visible light assisted dye degradation, *Process Saf. Environ. Prot.*, 161 (2022) 703–722.
- [23] P. Ahuja, S.K. Ujjain, R. Kanojia, P. Attri, Transition metal oxides and their composites for photocatalytic dye degradation, *J. Compos. Sci.*, 5 (2021) 683–711.
- [24] K. Zhang, K.M. Parker, Halogen radical oxidants in natural and engineered aquatic systems, *Environ. Sci. Technol.*, 52 (2018) 9579–9594.
- [25] M. Wang, W. Zhen, B. Tian, J. Ma, G. Lu, The inhibition of hydrogen and oxygen recombination reaction by halogen atoms on over-all water splitting over Pt-TiO₂ photocatalyst, *Appl. Catal., B*, 236 (2018) 240–252.
- [26] Y. Tu, W. Tang, Y. Li, J. Pu, J. Liao, W. Wu, S. Tian, Insights into the implication of halogen ions on the photoactivity of dissolved black carbon for the degradation of pharmaceutically active compounds, *Sep. Purif. Technol.*, 300 (2022) 121–765.
- [27] Z. Huang, H. Bao, Y. Yao, W. Lu, W. Chen, Novel green activation processes and mechanism of peroxymonosulfate based on supported cobalt phthalocyanine catalyst, *Appl. Catal., B*, 154–155 (2014) 36–43.
- [28] H.T. Pham, K. Suto, C. Inoue, Trichloroethylene transformation in aerobic pyrite suspension: pathways and kinetic modeling, *Environ. Sci. Technol.*, 43 (2009) 6744–6749.
- [29] T.T. Tsai, C.M. Kao, T.Y. Yeh, M.S. Lee, Chemical oxidation of chlorinated solvents in contaminated groundwater: review, *Pract. Period. Hazard. Toxic Radioact. Waste Manage.*, 12 (2008) 116–126.
- [30] G.P. Anipsitakis, D.D. Dionysiou, Radical generation by the interaction of transition metals with common oxidants, *Environ. Sci. Technol.*, 28 (2004) 3705–3712.
- [31] S. Chen, J. Hu, L. Lu, L. Wu, Z. Liang, J. Tang, H. Hou, S. Liang, J. Yang, Iron porphyrin-TiO₂ modulated peroxymonosulfate activation for efficient degradation of 2,4,6-trichlorophenol with high-valent iron-oxo species, *Chemosphere*, 309 (2022) 136744, doi: 10.1016/j.chemosphere.2022.136744.
- [32] D. Ouyang, Y. Chen, J. Yan, L. Qian, L. Han, M. Chen, Activation mechanism of peroxymonosulfate by biochar for catalytic degradation of 1,4-dioxane: important role of biochar defect structures, *Chem. Eng. J.*, 370 (2019) 614–624.
- [33] H. Li, C. Shan, W. Li, B. Pan, Peroxymonosulfate activation by iron(III)-tetraamidomacrocyclic ligand for degradation of organic pollutants via high-valent iron-oxo complex, *Water Res.*, 147 (2018) 233–241.
- [34] D.S. Su, S. Perathoner, G. Centi, Nanocarbons for the development of advanced catalysts, *Chem. Rev.*, 113 (2013) 5782–5816.
- [35] D.S. Su, J. Zhang, B. Frank, A. Thomas, X. Wang, J. Paraknowitsch, R. Schlögl, Metal-free heterogeneous catalysis for sustainable chemistry, *ChemSusChem*, 3 (2010) 169–180.
- [36] H. Liu, Y. Liu, D. Zhu, Chemical doping of graphene, *J. Mater. Chem.*, 21 (2011) 3335–3345.
- [37] D. Deng, X. Pan, L. Yu, Y. Cui, Y. Jiang, J. Qi, W.-X. Li, Q. Fu, X. Ma, Q. Xue, G. Sun, X. Bao, Toward N-doped graphene via solvothermal synthesis, *Chem. Mater.*, 23 (2011) 1188–1193.
- [38] Y. Gao, G. Hu, J. Zhong, Z. Shi, Y. Zhu, D.S. Su, J. Wang, X. Bao, D. Ma, Nitrogen-doped sp²-hybridized carbon as a superior catalyst for selective oxidation, *Angew. Chem. Int. Ed. Engl.*, 52 (2013) 2109–2113.
- [39] D.H. Guo, R. Shibuya, C. Akiba, S. Saji, T. Kondo, J. Nakamura, Active sites of nitrogen-doped carbon materials for oxygen reduction reaction clarified using model catalysts, *Science*, 351 (2016) 361–365.
- [40] P. Liang, C. Zhang, X. Duan, H. Sun, S. Liu, M.O. Tade, S. Wang, An insight into metal organic framework derived N-doped graphene for the oxidative degradation of persistent contaminants: formation mechanism and generation of singlet oxygen from peroxymonosulfate, *Environ. Sci.: Nano*, 4 (2017) 315–324.
- [41] K. Zhou, W. Zhou, X. Liu, Y. Wang, J. Wan, S. Chen, Nitrogen self-doped porous carbon from surplus sludge as metal-free electrocatalysts for oxygen reduction reactions, *ACS Appl. Mater. Interfaces*, 6 (2014) 14911–14918.
- [42] H. Sun, S. Liu, G. Zhou, H.M. Ang, M.O. Tade, Wang, S. Reduced graphene oxide for catalytic oxidation of aqueous organic pollutants, *ACS Appl. Mater. Interfaces*, 4 (2012) 5466–5471.
- [43] X. Duan, Z. Ao, H. Sun, S. Indrawirawan, Y. Wang, J. Kang, F. Liang, Z.H. Zhu, S. Wang, Nitrogen-doped graphene for generation and evolution of reactive radicals by metal-free catalysis, *ACS Appl. Mater. Interfaces*, 7 (2015) 4169–4178.
- [44] Z. Luo, S. Lim, Z. Tian, J. Shang, L. Lai, B. MacDonald, C. Fu, Z. Shen, T. Yu, J. Lin, Pyridinic N doped graphene: synthesis, electronic structure, and electrocatalytic property, *J. Mater. Chem.*, 21 (2011) 8038–8044.
- [45] J. Long, X. Xie, J. Xu, Q. Gu, L. Chen, X. Wang, Nitrogen-doped graphene nanosheets as metal-free catalysts for aerobic selective oxidation of benzylic alcohols, *ACS Catal.*, 2 (2012) 622–631.
- [46] Y. Zhou, J. Jiang, Y. Gao, J. Ma, S.Y. Pang, J. Li, X.T. Lu, L.P. Yuan, Activation of peroxymonosulfate by benzoquinone: a novel nonradical oxidation process, *Environ. Sci. Technol.*, 49 (2015) 12941–12950.
- [47] D. Zhou, L. Chen, C. Zhang, Y. Yu, L. Zhang, F. Wu, A novel photochemical system of ferrous sulfite complex: kinetics and mechanisms of rapid decolorization of Acid Orange 7 in aqueous solutions, *Water Res.*, 57 (2014) 87–95.
- [48] Z.J. Lu, S.J. Bao, Y.T. Gou, C.J. Cai, C.C. Ji, M.W. Xu, J. Song, R. Wang, Nitrogen-doped reduced-graphene oxide as an efficient metal-free electrocatalyst for oxygen reduction in fuel cells, *RSC Adv.*, 3 (2013) 3990–3995.
- [49] D. Geng, Y. Chen, Y. Chen, Y. Li, R. Li, X. Sun, S. Ye, S. Knights, High oxygen-reduction activity and durability of nitrogen-doped graphene, *Energy Environ. Sci.*, 4 (2011) 760–764.
- [50] T.C. Nagaiah, S. Kundu, M. Bron, M. Muhler, W. Schuhmann, Nitrogen-doped carbon nanotubes as a cathode catalyst for the oxygen reduction reaction in alkaline medium, *Electrochem. Commun.*, 12 (2010) 338–341.
- [51] L. Zhang, J. Niu, M. Li, Z. Xia, Catalytic Mechanisms of sulfur-doped graphene as efficient oxygen reduction reaction catalysts for fuel cells, *J. Phys. Chem.*, 118 (2014) 3545–3553.
- [52] T. Enoki, S. Fujii, K. Takai, Zigzag and armchair edges in graphene, *Carbon*, 50 (2012) 3141–3145.
- [53] G. Lee, K. Cho, Electronic structures of zigzag graphene nanoribbons with edge hydrogenation and oxidation, *Phys. Rev. B*, 79 (2009) 165440, doi: 10.1103/PhysRevB.79.165440.
- [54] J. Chen, X.W. Dong, S.S. Cao, L.Y. Zhu, Z.H. Song, J. Jin, H.X. Yang, Preparation of activated carbon from sludge by ‘double green activation’ and adsorption capacity for Congo red dye, *Desal. Water Treat.*, 249 (2022) 61–73.
- [55] J. Chen, L.Y. Zhu, S.S. Cao, Z.H. Song, X.H. Yang, J. Jin, Z.M. Chen, Activating peroxymonosulfate using carbon from cyanobacteria as support for zero-valent iron, *Environ. Sci. Pollut. Res.*, 29 (2022) 73353–73364.
- [56] R.V. Khose, K.D. Lokhande, M.A. Bhakare, P.S. Dhumal, P.H. Wadekar, S. Some, Boron nitride doped chitosan functionalized graphene for an efficient dye degradation, *Chem. Select*, 6 (2021) 7956–7963.